Check for updates

NANO · MICRO small
www.small-journal.com

Lithium Azides Induced SnS Quantum Dots for Ultra-Fast and Long-Term Sodium Storage

*Qiaohuan Cheng, Yingxue Li, Panyu Gao, Guanglin Xia, Shengnan He, Yaxiong Yang, Hongge Pan, and Xuebin Yu**

Tin sulfide (SnS) is an attractive anode for sodium ion batteries (NIBs) because of its high theoretical capacity, while it seriously suffers from the inherently poor conductivity and huge volume variation during the cycling process, leading to inferior lifespan. To intrinsically maximize the sodium storage of SnS, herein, lithium azides (LiN_3)-induced SnS quantum dots (QDs) are first reported using a simple electrospinning strategy, where SnS QDs are uniformly distributed in the carbon fibers. Taking the advantage of LiN_3, which can effectively prevent the growth of crystal nuclei during the thermal treatment, the well-dispersed SnS QDs performs superior Na^+ transfer kinetics and pseudocapacitive when used as an anode material for NIBs. The 3D SnS quantum dots embedded uniformly in N-doped nanofibers (SnS QDs@NCF) electrodes display superior long cycling life-span (484.6 mAh g^{-1} after 5800 cycles at 2 A g^{-1} and 430.9 mAh g^{-1} after 7880 cycles at 10 A g^{-1}), as well as excellent rate capability (422.3 mAh g^{-1} at 20 A g^{-1}). This fabrication of transition metal sulfides QDs composites provide a feasible strategy to develop NIBs with long life-span and superior rate capability to pave its practical implementation.

1. Introduction

Sodium ion batteries (NIBs) are the promising alternative candidate to lithium-ion batteries (LIBs) owing to the cost-effective and highly available sodium resources accompanied with similar energy storage mechanisms to LIBs.[1,2] However, the active materials those display superior Li-ion storage capabilities may have compromised performances in NIBs, taking conventional graphite anodes as an example, which is largely attributed to the sluggish kinetics and huge volume expansion bestowed by the larger radius of Na^+ (1.02 Å) than that of Li^+ (0.76 Å).[3,4] Among the reported electrode materials, the ones combined with conversion and alloys-type have been considered as one of the most feasible candidates owing to their higher theoretical capacity than that of others, e.g., alloys-type (Sb, Sb et al.),[5,6] intercalation-type (graphite, $MoSe_2$, MoS_2 et al.),[7,8] and conversion-type (FeS_2, Co_9S_8 et al.).[9–11] Typically, tin sulfide (SnS) has drawn intensive interests in NIBs because of the large interlayer spacing (4.33 Å), which can accommodate the fast Na-ion diffusion, high theoretical capacity (1022 mAh g^{-1}), and environmental friendless, as well as the sources availability.[12,13] Specially, the relatively weaker Sn–S bonds compared with metal oxides boost the kinetics of the conversion reaction.[14] Regrettably, SnS still suffers from limited sodium storage properties caused by the poor electrical conductivity and substantial volumetric fluctuations resulted in severe structural degradation and instability of the solid-electrolyte interphase (SEI).[15]

Previous studies have demonstrated that nanostructure design, particularly for quantum-dots (QDs) that lead to much less strain according to the reported computational results, is an effective strategy to enhance the sodium storage properties, which can effectively facilitate the Na^+ diffusion kinetics as the conducting and diffusion pathways for electrons and ions are significantly shortened, as well as tolerate the huge dimensional strains without fragmentation, thus greatly enhancing the electrochemical reactivity of electrode materials.[16–18] Nonetheless, previous report on SnS-based anodes are mainly focused on manipulating in morphology modification, simple hybridization with carbon materials, as well as heterostructure without involving the effect of particle size.[19–21] Besides, the traditional synthetic approaches, hydro/solvothermal method, direct deposition, polyol process, and mechanical milling methods, have limitations in the fabrication of SnS QDs.[22–24] Other challenges lie in that QDs with the large surface area are unstable and vulnerable, which are prone to self-aggregation during the electrochemical reaction.[25] Moreover, the unstable SEI formed by excess consumption of Na metal and the electrolyte is inevitable due to continuously exposed the new surface of the material to the electrolyte, leading to the fast capacity decay and low Coulombic efficiencies during the repetitive discharge–charge process.[26,27]

Q. Cheng, Y. Li, P. Gao, G. Xia, X. Yu
Department of Materials Science
Fudan University
Shanghai 200433, China
E-mail: yuxuebin@fudan.edu.cn
S. He, Y. Yang, H. Pan
Institute of Science and Technology for New Energy
Xi'an Technological University
Xi'an 710021, China

The ORCID identification number(s) for the author(s) of this article can be found under https://doi.org/10.1002/smll.202302188

DOI: 10.1002/smll.202302188

 © 2023 Wiley-VCH GmbH

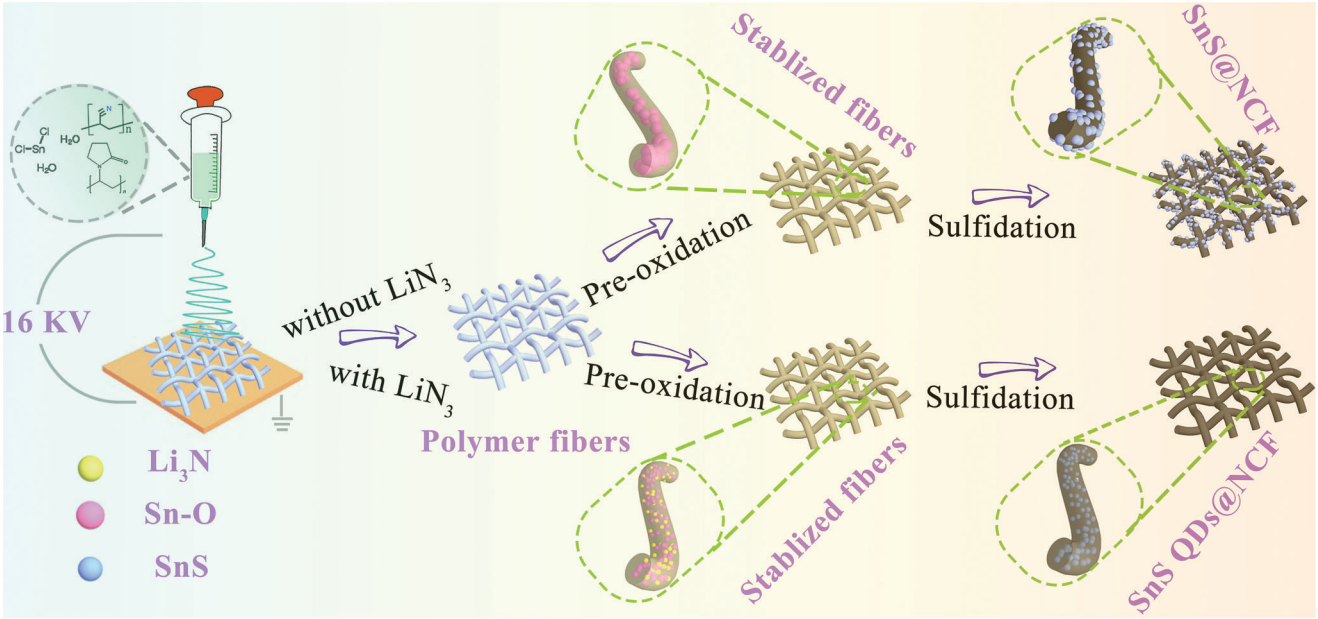

Figure 1. Schematic illustration of the fabrication process of SnS QDs@NCF and SnS@NCF.

Integrating QDs with electronically carbon buffer/matrix can be an advanced strategy to undermine the above deficiency for QDs.[28–31] Various carbonaceous materials, such as graphene and amorphous carbon, have been adopted as a buffer matrix for QDs composites to enhance electrically conductivity, alleviate volume changes and protect active materials from contacting directly with electrolyte.[32,33] Hence, a robust and well-dispersed SnS QDs structure is necessary to lead to more-improved characteristics due to the enhanced structural damage tolerance, keeping the electrode integrity during cycling.

The nucleation/growth of particles can be obstructed by introducing effective inhibitors/additives during thermal decomposition, which is also named as growth inhibition mechanism, while eventually leading to the formation of subnano-sized particles during thermal decomposition.[34,35] Hence, it is expected that the well-dispersed SnS QDs would be generated by the inhibitors-assisted strategy. In this paper, SnS quantum dots embedded uniformly in N-doped carbon nanofibers (SnS QDs@NCF) were fabricated via a simple electrospinning process. In this strategy, lithium azides served as inhibitors were decomposed during pre-oxidation process, resulting in strong repulsive forces which can prevent the growth of crystal nuclei during the thermal treatment. Upon testing as NIBs, a stable long-term cycling at high rate is obtained, and the optimized desirable SnS QDs@NCF delivers a high capacity of 430.9 mAh g^{-1} after 7880 cycles with a Coulombic efficiency of almost 100% at 10 A g^{-1}. The favorable construction approach in this paper will bring inspiration for other transition metal sulfide QDs composites, providing a facial direction for fabricating the high-performance anode for next-generation energy storage system.

2. Results and Discussion

The synthetic process of SnS@NCF and SnS QDs@NCF is illustrated in **Figure 1**. After the electrospinning process, the white Sn-containing polymeric nanofibers with or without LiN_3 are obtained, subsequently, the SnS@NCF and SnS QDs@NCF are obtained by pre-oxidation and following sulfidation treatment, respectively. There is no obvious difference in morphologies between the pre-oxidized polymeric nanofibers with or without LiN_3, as demonstrated in Figure S1 (Supporting Information), both the nanofibers show relatively smooth surface. It deserves to mention that, during the pre-oxidation process, LiN_3 undergoes a violent decomposition process that creates a strong repulsive force, which can prevent the Sn–O intermediate from agglomerating and growing into large particles during the following sulfidation process, resulting in the formation of SnS QDs distributed homogeneously in the N-doped carbon fibers (SnS QDs@NCF).

The morphologies of the SnS QDs@NCF and SnS@NCF are characterized by field-emission scanning electron microscopy (FESEM) and transmission electron microscopy (TEM). As depicted in **Figure 2**a,b and Figure S2 (Supporting Information), the as-spun SnS@NCF is highly uniform with an average diameter of 96 nm, and the dense nanoparticles are formed on the surface of the cross-linked fibers, resulting in the rough surface. Besides, the nanoparticles with the diameter of 10 (± 5) nm are exposed to the surface of the fibers, as shown in the magnified TEM images (Figure 2c). The clearly lattice fringes can be observed in the inset of Figure 2c, where the interplanar spacing of 0.155 nm can be assigned to the (250) planes of SnS. The selected area diffraction (SAED) image in Figure 2d shows concentric diffraction rings, which can be well assigned to the (120), (111), (211), and (142) planes of SnS.

As for the optimized SnS QDs@NCF, it presents the typical appearance of electrospun fibers with smooth surface and an average diameter of 78 nm (Figure 2e; Figure S3, Supporting Information), which is thinner than that of SnS@NCF due to the absence of particles on the surface of fibers. TEM images in Figure 2f demonstrate that there are no particles can be observed throughout the whole fibers, and SnS QDs with an average size of

 © 2023 Wiley-VCH GmbH

16136829, 0, Downloaded from https://onlinelibrary.wiley.com/doi/10.1002/smll.202302188 by Fudan University, Wiley Online Library on [03/06/2023]. See the Terms and Conditions (https://onlinelibrary.wiley.com/terms-and-conditions) on Wiley Online Library for rules of use; OA articles are governed by the applicable Creative Commons License

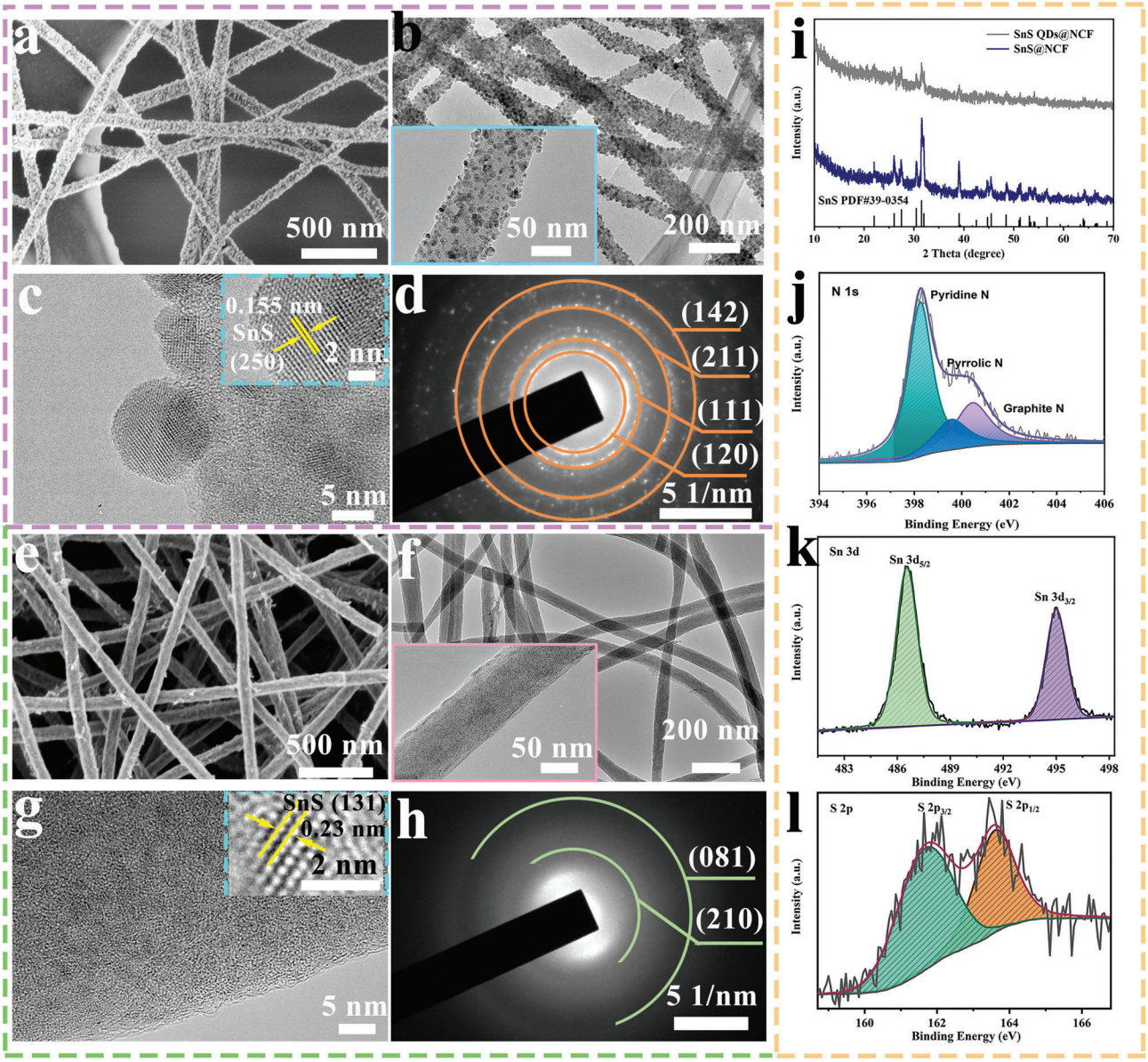

Figure 2. SnS@NCF of a) SEM images, b) TEM images, c) HRTEM images, and d) SAED pattern. SnS QDs@NCF of e) SEM images, f) TEM images, g) HRTEM images, and h) SAED pattern. i) XRD patterns of SnS@NCF and SnS QDs@NCF, j) N 1s, k) Sn 3*d*, and l) S 2*p* XPS spectrum of SnS QDs@NCF.

2 nm are homogeneously confined within the fibers, and the interplanar spacing of 0.23 nm can be assigned to the (131) planes of SnS (Figure 2g).[36] Besides, the SAED in Figure 2h discloses the poor crystal quality due to the quantum size effect, and the ring-like diffractions are well consistent to the (210) and (081) crystal planes of SnS.

As demonstrated in Figure 2i, X-ray diffraction (XRD) patterns of SnS@NCF and SnS QDs@NCF reveal that all diffraction peaks can be indexed to the orthorhombic structure of SnS (JCPDS: 39-0354). Clearly, SnS QDs@NCF exhibit broader diffraction peaks compared to the SnS@NCF, indicating the tiny particles existed in SnS QDs@NCF.[26] Subsequently, Raman spectra is carried out to characterize SnS QDs@NCF composites, the intense peaks at 1350 and 1575 cm^{-1} are assigned to the D band (disorder-induced structure) and G band (graphitic-induced structure), respectively (Figure S4, Supporting Information).[37] The intensity of D band is much higher than that of G band, suggesting an amount of defects and the disordering degree are involved in fibers, which can offer abundant accessible pathways for Na-ion transport.[38] Furthermore, the carbon content of SnS QDs@NCF can be determined to be 51.1% based on the TGA results (Figure S5, Supporting Information). The hybrids (SnS QDs@NCF-1, SnS QDs@NCF-2, and SnS QDs@NCF-3) with different carbon content are also characterized (Figure S6, Supporting Information).

Furthermore, the valence states and electronic structure of the as-synthesized SnS QDs@NCF are revealed by X-ray photoelectron spectroscopy (XPS). As displayed in the full survey scan spectrum (Figure S7, Supporting Information), a pronounced N 1*s* peak can be observed, which can also be detected in the survey

 © 2023 Wiley-VCH GmbH

16136829, 0, Downloaded from https://onlinelibrary.wiley.com/doi/10.1002/smll.202302188 by Fudan University, Wiley Online Library on [03/06/2023]. See the Terms and Conditions (https://onlinelibrary.wiley.com/terms-and-conditions) on Wiley Online Library for rules of use; OA articles are governed by the applicable Creative Commons License

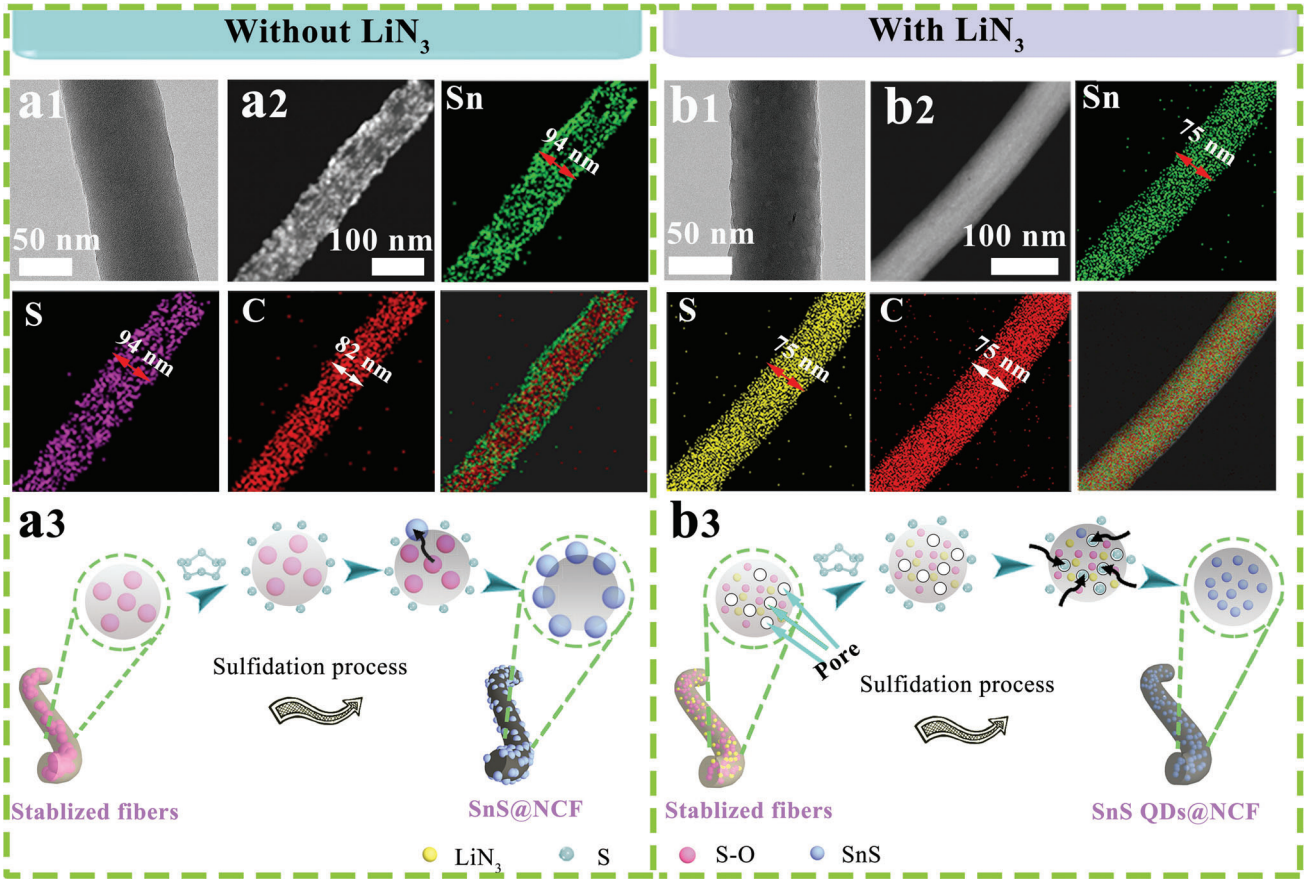

Figure 3. SnS@NCF: a1) TEM image of stabilized fibers after pre-oxidation; a2) STEM image and the corresponding elemental mapping images of Sn, S, and C; a3) Reaction mechanism without LiN_3. SnS QDs@NCF: b1) TEM image of stabilized fibers after pre-oxidation; b2) STEM image and the corresponding elemental mapping images of Sn, S, and C; b3) Reaction mechanism with LiN_3.

scan spectrum of SnS@NCF (Figure S8a, Supporting Information). The high-resolution N 1*s* spectrum for SnS QDs@NCF (Figure 2j) can be deconvoluted into three peaks: pyridinic N (398.3 eV), pyrrolic N (399.8 eV), and graphitic N (401.1 eV), which are consistent with that of SnS@NCF (Figure S8b, Supporting Information), indicating that the N element in the composites is attributed to the decomposition of polymer precursor (polyvinyl pyrrolidone and polyacrylonitrile).[39] The incorporated N element in carbon nanofibers is expected to increase the electrical conductivity and the specific capacity by producing abundant defects or active sites.[40] Besides, the oxygen of composites can be attributed to the pre-oxidation process, which can strength the fibers integrity and continuity.[41] The Sn 3*d* XPS spectrum presents two peaks located at 486.7 and 495.2 eV, which correspond to the Sn $3d_{5/2}$ and Sn $3d_{3/2}$, respectively, confirming the chemical state of Sn^{2+} in SnS (Figure 2k).[42] The high-resolution S 2*p* spectrum is shown in Figure 2l, in which the peaks with binding energy of 161.6 and 163.6 eV correspond to S $2p_{3/2}$ and S $2p_{1/2}$, respectively, suggesting the successful formation of the SnS phase. The C 1*s* spectrum (Figure S9, Supporting Information) can be deconvoluted into four peaks centered at 284.7, 285.9, 288.3, and 289.9 eV, corresponding to C–C, C–N/C–S, C=O, and O–C=O, respectively, which also demonstrates the existence of N doped sites on the carbon fibers.[43,44]

Figure 3 schematically shows the reaction mechanisms of SnS@NCF and SnS QDs@NCF. Figure 3a1,b1 exhibits the TEM images of stabilized fibers after pre-oxidation of SnS@NCF and SnS QDs@NCF, respectively. Figure 3b1 clearly shows the pore structure which is different from the stabilized fibers of SnS@NCF (Figure 3a1). The corresponding scanning TEM (STEM) and EDS elemental mapping analysis in Figure 3a2 and Figure S10 (Supporting Information) indicate the presence of N element and the distribution state of Sn, S, C, and N elements, where the Sn element is well coincided with S, but shows higher concentration in the outer layer of fibers than that of C and N, indicating that the small SnS particles are mainly grown on the surface of N-doped carbon fibers. In contrast, the EDS elemental mapping analysis in Figure 3b2 and Figure S11 (Supporting Information) confirm the coexistence and homogenous distribution of Sn, S, C, and N, suggesting that the SnS QDs are homogeneously distributed in the N-doped carbon fibers. As a result, the reaction mechanism can be clarified as Figure 3a3,b3. As the LiN_3 forms a strong vapor phase in the process of violent decomposition process which prompts the formation of abundant pore inside the nanofibers, the stabilized fibers of SnS QDs@NCF precursors after pre-oxidation exhibits pore structure. All of these processes further prevented the Sn–O intermediate from agglomerating and

 © 2023 Wiley-VCH GmbH

16136829, 0, Downloaded from https://onlinelibrary.wiley.com/doi/10.1002/smll.202302188 by Fudan University, Wiley Online Library on [03/06/2023]. See the Terms and Conditions (https://onlinelibrary.wiley.com/terms-and-conditions) on Wiley Online Library for rules of use; OA articles are governed by the applicable Creative Commons License

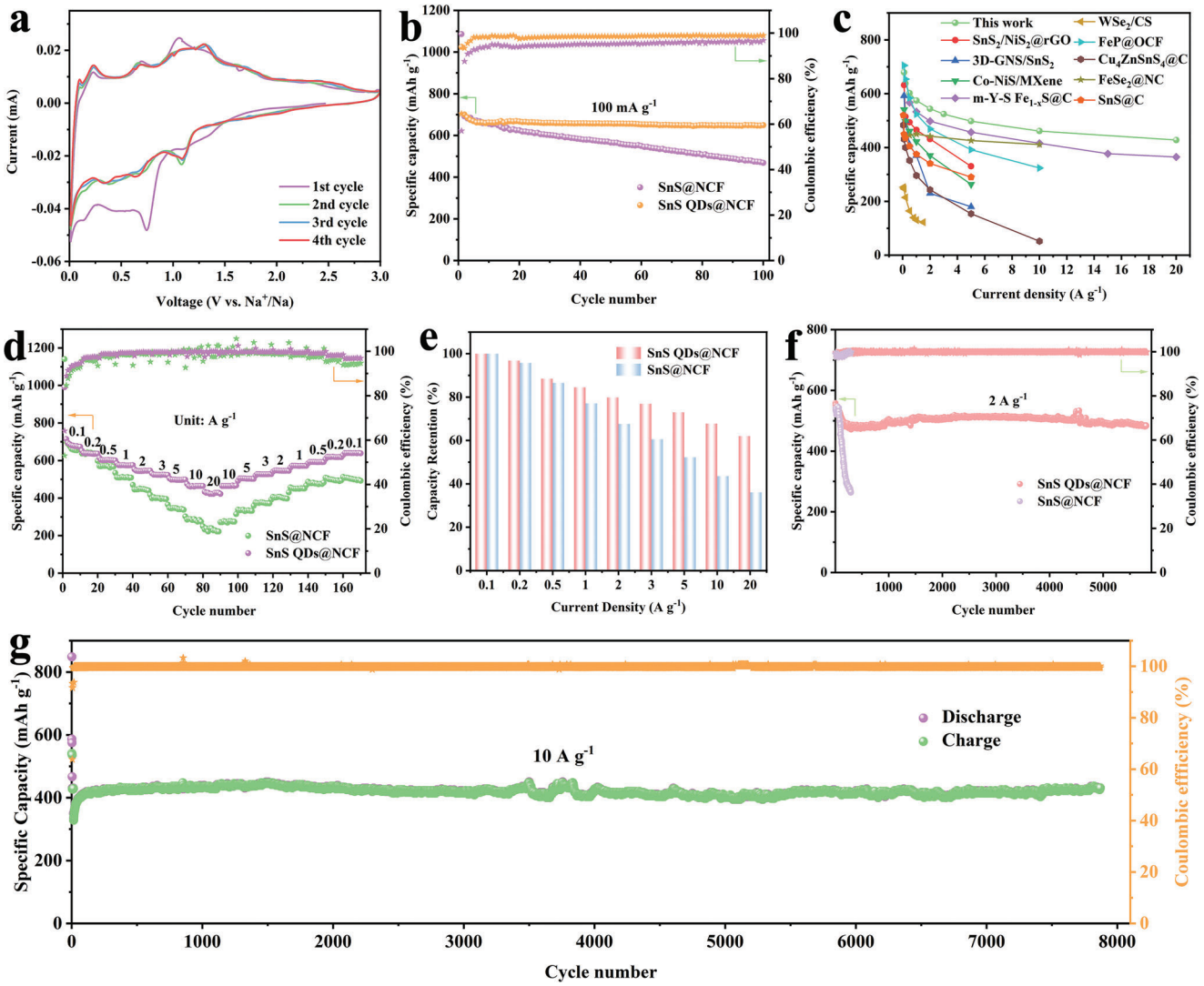

Figure 4. a) CV curves of SnS QDs@NCF at 0.1 mV s^{-1}. b) Cycling performance at 100 mA g^{-1} for SnS@NCF and SnS QDs@NCF. c) A comparison of the electrochemical performance metrics of SnS QDs@NCF electrode with representative anodes reported. d) Rate performance of SnS@NCF and SnS QDs@NCF. e) Capacity Retention of the active material of the SnS QDs@NCF electrode and SnS@NCF electrode at different charge–discharge current densities versus the specific capacity at 0.1 A g^{-1}. f) Cycling performance at 2 A g^{-1} for SnS@NCF and SnS QDs@NCF. g) Long-term cycle stability of SnS QDs@NCF at high current density of 10 A g^{-1}.

growing into large particles during the following sulfidation process.

In the following sulfidation process, the S can diffuse into the pores, forming SnS nanocrystallines within the fibers, while for the sample without LiN_3, the S surrounds the surface of the fiber, and Sn have to diffuses outward to react with S, leading to SnS nanoparticles formed on the surface of the fiber.

To comprehensive understand the sodium-storage mechanism, the electrochemical analysis is necessary. **Figure 4**a performs the cyclic voltammetry (CV) curves of SnS QDs@NCF for the first four cycles in the voltage window between 0.01 and 3 V at a scan rate of 0.1 mV s^{-1}. For the first sodiation process, a significant reduction peak appears at 0.75 V and disappears at the subsequent cycles, which is attributed to the formation of the solid electrolyte interface (SEI) layer and the conversion reaction of SnS to Sn and Na_2S according to the previous reports.[12,26]

$$SnS + 2Na^+ + 2e^- \rightarrow Na_2S + Sn \quad (1)$$

And then the small reduction peaks positioned at 0.4 and 0.14 V correspond to the multi-step alloying reaction of Na and Sn.[20,34]

$$Sn + xNa^+ + xe^- \rightarrow Na_xSn \quad (2)$$

These peaks shift positively to 1.1, 0.7, and 0.3 V, respectively, from the second sodiation process, which is called activation process.[28] For the first desodiation process, the peaks at 0.2 and 0.6 V are considered as multi-step dealloying of Na_xSn, a strong peak at 1.1 V is related to the reverse conversion

© 2023 Wiley-VCH GmbH

16136829, 0, Downloaded from https://onlinelibrary.wiley.com/doi/10.1002/smll.202302188 by Fudan University, Wiley Online Library on [03/06/2023]. See the Terms and Conditions (https://onlinelibrary.wiley.com/terms-and-conditions) on Wiley Online Library for rules of use; OA articles are governed by the applicable Creative Commons License

reaction from Sn to SnS, which means the reversible redox process for SnS QDs@NCF.[25,27] In the subsequent cycles, a pair of reduction/oxidation peaks located at 1.1 V/1.3 V are related to the mutually redox reaction between SnS and Sn, and the reduction peaks of 0.3 and 0.7 V, the oxidation peaks of 0.1 and 0.2 V, as well as 0.6 V can be assigned to the multi-step alloying and dealloying between Sn and Na_xSn.[41] Besides, the CV profiles are overlapped, indicating an excellent reversibility and stability for Na^+ storage. The CV curves of SnS@NCF are also investigated. The two reduction peaks appearing below ≈0.75 V are observed for SnS QDs@NCF, but not for SnS@NCF during the first cycle, which can be attributed to the effect of quantum dots size. Furthermore, SnS QDs@NCF shows obviously multi-step alloying of Na and Sn at 0.4 and 0.14 V, and the SnS@NCF with large particle size of SnS performs a chaos alloying reaction, besides, the CV curves of SnS@NCF displays poor overlap (Figure S12, Supporting Information).[40]

The cycling stability is first investigated at 100 mA g^{-1} ≈0.1C (1 C = 1022 mA g^{-1} according to the theoretical capacity of SnS). As presented in Figure 4b, it is obviously that SnS@NCF performs dramatic capacity fading from the first cycle onward, delivering a relatively low capacity (472.2 mAh g^{-1}) after 100 cycles, corresponding to a low capacity retention ratio of 70.3% (compared with the 5th cycle). While a good cycling stability is detected for SnS QDs@NCF, which gives a reversible discharge capacity of 651.2 mAh g^{-1} after 100 cycles, corresponding to a high capacity retention ratio of 97.4%. The cycling stability is further illuminated by the discharge–charge profile. As displayed in Figure S13a (Supporting Information), the initial discharge capacity is greater than that of charge capacity, the irreversible sodium storage caused by the formation of solid state electrolyte interfaces (SEI) for the first sodiation process can be responsible for the low initial coulombic efficiency. And the discharge–charge profiles almost overlapping from the 2nd cycle onward, presenting a highly reversible and stable cycling performance of SnS QDs@NCF. Besides, the sodiation–desodiation plateaus is accordance well with the CV curve results. However, as demonstrated in Figure S14 (Supporting Information), the discharge–charge profiles of SnS@NCF show obvious capacity decay per cycle, demonstrating the capacity fade rapidly.

The rate capability is also performed to evaluate the Na-ion storage kinetics. The discharge/charge curves of SnS QDs@NCF at different rates are displayed in Figure S13b (Supporting Information). As shown in Figure 4d, the two electrodes display the pretty much comparative capacity at current density of 0.1 and 0.2 A g^{-1}, however, SnS QDs@NCF exhibits a better rate capability than that of SnS@NCF from the current density of 0.5 A g^{-1} onward. SnS QDs@NCF performs discharge capacities of 602.3, 575.2, 543.5, 523.6, 496.6, and 463.9 mAh g^{-1} at 0.5, 1, 2, 3, 5, and 10 A g^{-1}, respectively. A relatively high reversible capacity of 422.3 mAh g^{-1} can be retained even at 20 A g^{-1}, which is much higher than that of SnS@NCF (227.6 mAh g^{-1}). When the current density returns to 0.1 A g^{-1}, a reversible capacity of 640.2 mAh g^{-1} can still be achieved for SnS QDs@NCF even after 160 cycles at current density ranging from 0.1 to 20 A g^{-1}, while SnS@NCF performs a limited capacity of 496.7 mAh g^{-1}, suggesting the high-rate capability of SnS QDs@NCF.

The capacity retention can be estimated by normalizing the specific capacity of the electrode at different current densities versus the specific capacity at 0.1 A g^{-1}, as shown in Figure 4e.[45] It can be observed that the active-material utilization of both SnS QDs@NCF and SnS@NCF decreases with increasing current density, while the utilization of SnS QDs@NCF is always higher than that of SnS@NCF. The significant enhanced utilization in SnS QDs@NCF electrode indicates the superior high-rate performance, as well as the improved electrical conductivity.

Intrigued by the excellent rate capability, the high-rate cycling stability is further evaluated at 2 and 10 A g^{-1}. As shown in Figure 4f, the SnS QDs@NCF delivers a reversible capacity of 484.6 mAh g^{-1} after 5800 cycles at 2 A g^{-1}, while SnS@NCF decreases to 265.6 mAh g^{-1} after 300 cycles. Considering the contribution of carbon nanofibers for Na^+ storage, the rate-performance and the cycling performance of NCF at a current density of 2 A g^{-1} are also tested (Figure S15a,b, Supporting Information). NCF performs discharge capacities of 317, 298.5, 266.4, 234.2, 204.8, 179.5, 162.5, 127.6, and 89.2 mAh g^{-1} at 0.1, 0.2, 0.5, 1, 2, 3, 5, 10, and 20 A g^{-1}, respectively. It exhibits excellent cycling stability with a limited capacity retention of 202.8 mAh g^{-1} and the slight increase in the discharge capacity after 500 cycles. This increase in capacity with cycles can be attributed that electrolyte reactions, and the electrode material can be constantly activated which improves reaction kinetics with increased interfacial compatibility between the electrolyte and the electrode material or the interfacial Na storage.[46] All the above results indicate that the NCF only contributes a small amount of capacity to SnS QDs@NCF. Impressively, when the current density increases to 10 A g^{-1}, the SnS QDs@NCF electrode performs superior long-term cyclability with a reversible capacity of 430.9 mAh g^{-1} after 7880 cycles (Figure 4g), implying the robust structure during sodiation/desodiation process. The SnS@QDs@NCF electrode exhibited a capacity rise in the first few cycles. It can be attributed to the improvement of Na^+ accessibility and accommodation behavior in the electrode, and the charging capacity decrease after rise can be attributed to the stable formation of a gel-like film of the electrode.[47] Based on the above results, it can be concluded that SnS QDs@NCF electrode exhibits high capacity, superior rate capability, and ultra-stable cycling performance, which outperform most previously reported anodes for NIBs (Figure 4c), demonstrating the significant promotion for NIBs anodes.[16,48–55]

To further understand the electrochemical reaction mechanisms, the detailed kinetics analysis based on the CV tests is conducted for SnS QDs@NCF and SnS@NCF. **Figure 5**a displays the CV curves of SnS QDs@NCF electrodes at various scan rates from 0.1 to 1.2 mV s^{-1}. The CV curves preserve the basic shape and the intensities of reduction/oxidation peaks vary with the scan rate, indicating the slight polarization and good reversibility of SnS QDs@NCF.[56] Furthermore, the relationship between the scan rate (v) and the measured current (i) can be described by the formula:

$$i = av^b \tag{3}$$

$$\log i = b\log v + \log a \tag{4}$$

where a is constant, the b-value can be determined by the slope of log(v)–log(i) plots.[23,53] It is well known that b-value of 0.5 indicates a diffusion-controlled process, while for a surface-controlled process b-value is 1.0. In our case, the b-values for the

© 2023 Wiley-VCH GmbH

16136829, 0, Downloaded from https://onlinelibrary.wiley.com/doi/10.1002/smll.202302188 by Fudan University, Wiley Online Library on [03/06/2023]. See the Terms and Conditions (https://onlinelibrary.wiley.com/terms-and-conditions) on Wiley Online Library for rules of use; OA articles are governed by the applicable Creative Commons License

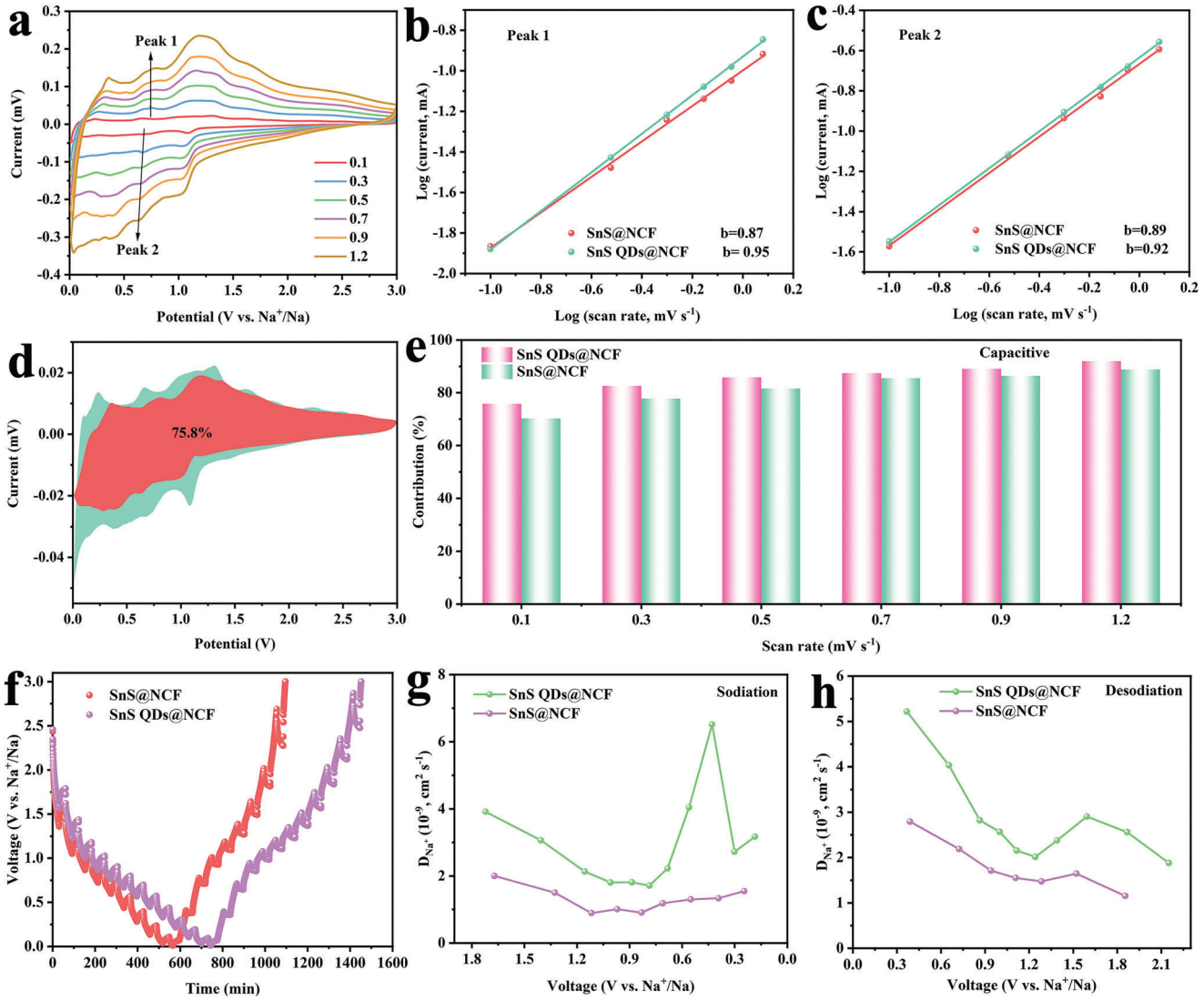

Figure 5. a) CV curves of SnS QDs@NCF at different scan rate; Log(i) versus Log(v) plots of b) SnS@NCF and c) SnS QDs@NCF; d) capacitive contribution of SnS QDs@NCF at 0.1 mV s^{-1}; e) ratio capacitive contribution for two electrodes at different scan rates; f) GITT potential profile of SnS@NCF and SnS QDs@NCF; diffusion coefficients of SnS@NCF and SnS QDs@NCF for g) sodiation and h) desodiation.

SnS QDs@NCF composites are calculated to be 0.95 and 0.92 corresponding to Peaks 1 and 2 (Figure 5b), respectively, indicating that diffusion-controlled and surface-controlled behavior synergistically dominate the charge storage. Meanwhile, the *b*-value of SnS@NCF is 0.87 and 0.89 for Peaks 1 and 2 (Figure 5c), respectively, which is lower than that of SnS QDs@NCF composites, implying that the enhanced capacitive kinetics behavior in SnS QDs@NCF through the effective structure optimization. The ratio of pseudocapacitive contribution can be quantitatively determined by the equation below:

$$i = k_1 v + k_2 v^{1/2} \tag{5}$$

where $k_1 v$ and $k_2 v_{1/2}$ correspond to the surface-controlled pseudocapacitive behavior and diffusion-controlled process, respectively.[57] The pseudocapacitive contribution for SnS QDs@NCF is identified as 75.8% (Figure 5d), much higher than that of SnS@NCF (70.2%) at 0.1 mV s^{-1} (Figures S16 and S17, Supporting Information), which is coincidence well with the *b*-value results, the higher *b*-value, the more pseudocapacitance reaction is dominant in charge storage behavior. Figure 5e shows the pseudocapacitive contributions for the two electrodes of SnS@NCF and SnS QDs@NCF at various scan rate. It is obvious that the pseudocapacitive effects enhanced with increasing the scan rate, but the pseudocapacitive contribution of two electrodes can always be ordered as follows: SnS QDs@NCF > SnS@NCF, suggesting the highly efficient absorption of Na^+ ions and fast sodiation/desodiation reaction kinetics for SnS QDs@NCF electrodes.[58] The large specific surface area of SnS QDs can be responsible for the high pseudocapacitive contribution, leading to fast sodium storage and high rate capacity.[56]

The SnS QDs@NCF and SnS@NCF electrodes are conducted in the electrochemical impedance spectroscopy (EIS) (Figure S18, Supporting Information). The smaller semicircles

 © 2023 Wiley-VCH GmbH

16136829, 0, Downloaded from https://onlinelibrary.wiley.com/doi/10.1002/smll.202302188 by Fudan University, Wiley Online Library on [03/06/2023]. See the Terms and Conditions (https://onlinelibrary.wiley.com/terms-and-conditions) on Wiley Online Library for rules of use; OA articles are governed by the applicable Creative Commons License

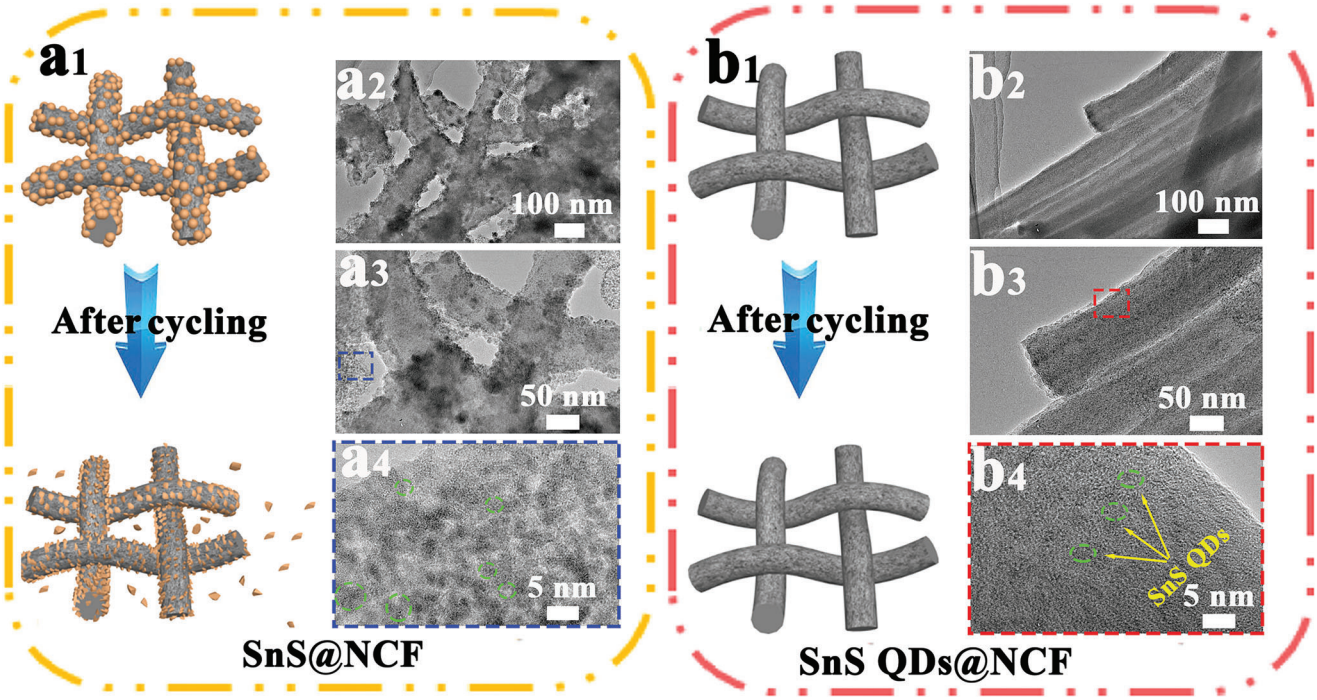

Figure 6. Schematic illustration of the morphology/structure evolutions during sodiation/desodiation process of a1) SnS@NG electrodes and b1) SnS QDs@NCF. TEM and HRTEM images of a2–a4) SnS@NCF and b2–b4) SnS QDs@NCF electrodes after 800 cycles at 2 A g^{-1}.

at the high-frequency and middle-frequency regions of SnS QDs@NCF represent the better conductivity and fast ion transport between the electrode and the electrolyte interface. Besides, to clarify the rate performance of SnS QDs@NCF and SnS@NCF on the view of the electrochemical point, the galvanostatic intermittent titration technique (GITT) (Figure 5f) is performed, which can be determined the sodium ion diffusion coefficient (D) according to the following equation:[59,60]

$$D = \frac{4}{\pi\tau}\left(\frac{m_m V_m}{M_s S}\right)^2\left(\frac{\Delta E_s}{\Delta E_\tau}\right)^2 \tag{6}$$

as shown in Figure 5g,h, the Na^+ diffusion coefficients of SnS QDs@NCF electrodes are higher than that of SnS@NCF at all voltage, which is in agreement with the results of rate performance, confirming the remarkably accelerated diffusion Na^+ due to the well-dispersed SnS QDs with highly grain refinement in conductive N-doped carbon nanofibers. The high Na-ion diffusion of SnS QDs@NCF indicates the superior sodium ion storage performances. The above pseudocapacitive calculation, EIS and GITT tests disclose that the SnS QDs@NCF electrode exhibits enhanced Na-ion transfer kinetics, thus resulting in the high-rate capability.

The morphology/structure evolution upon sodiation/desodiation process is performed through ex situ TEM observation, which further reveal the structure integrity of electrode. As illustrated in **Figure 6**a2–a4, the TEM and HRTEM images of SnS@NG electrodes after 800 cycles at 2 A g^{-1} reveal that the fibers still remain the original morphology, while the SnS particles grown on the fibers surface pulverize into smaller nanoparticles and even some nanoparticles detach from the fibers, which can be responsible for the drastic capacity fading during cycling process. For the cycled SnS QDs@NCF (Figure 6b2–b4), the SnS QDs are still firmly and uniformly confined into N-doped carbon nanofibers skeleton even after long-term cycling, resulting in excellent cycling stability. Based on the above results, the excellent Na^+ storage properties of SnS QDs@NCF composites can be attributed to the unique structure advantages, as illustrated in Figure 6a1,b1. First, the SnS QDs are homogeneously encapsulated into fibers, which are benefited for the ohm contact between active materials and carbon layers. Second, the conductive carbon layers protect SnS QDs from agglomeration during repeat sodiation/desodiation process, the SnS QDs still retain independent of each other even after hundreds of cycles. Third, the conductive shell can not only effectively relieve the stress concentration resulted from the volume expansion, but also enable stable SEI on the outer surface the whole structure, keeping the electrode structural integrity during ultrafast sodiation/desodiation process. Last but not least, the QDs are deemed to short ion/electron transfer path resulting in enhanced kinetics. By contrast, the SnS@NCF electrode composed of exposed and densely SnS particles (≈10 nm) on the surface of the fibers will be damaged after few cycles, in which the active materials SnS particles will be squeeze and destroy each other due to the stress accompanied volume expansion, thereby performing a rapid capacity fading.

Furthermore, to deepen understanding the structural stability of SnS QDs@NCF composite during cycling, finite element simulations were conducted to reveal the detailed stress distribution/change due to the sodiation-induced expansion. As shown in **Figure 7**a–d, two simplified models were carried out to simulate SnS@NCF and SnS QDs@NCF before and after sodiation

 © 2023 Wiley-VCH GmbH

16136829, 0, Downloaded from https://onlinelibrary.wiley.com/doi/10.1002/smll.202302188 by Fudan University, Wiley Online Library on [03/06/2023]. See the Terms and Conditions (https://onlinelibrary.wiley.com/terms-and-conditions) on Wiley Online Library for rules of use; OA articles are governed by the applicable Creative Commons License

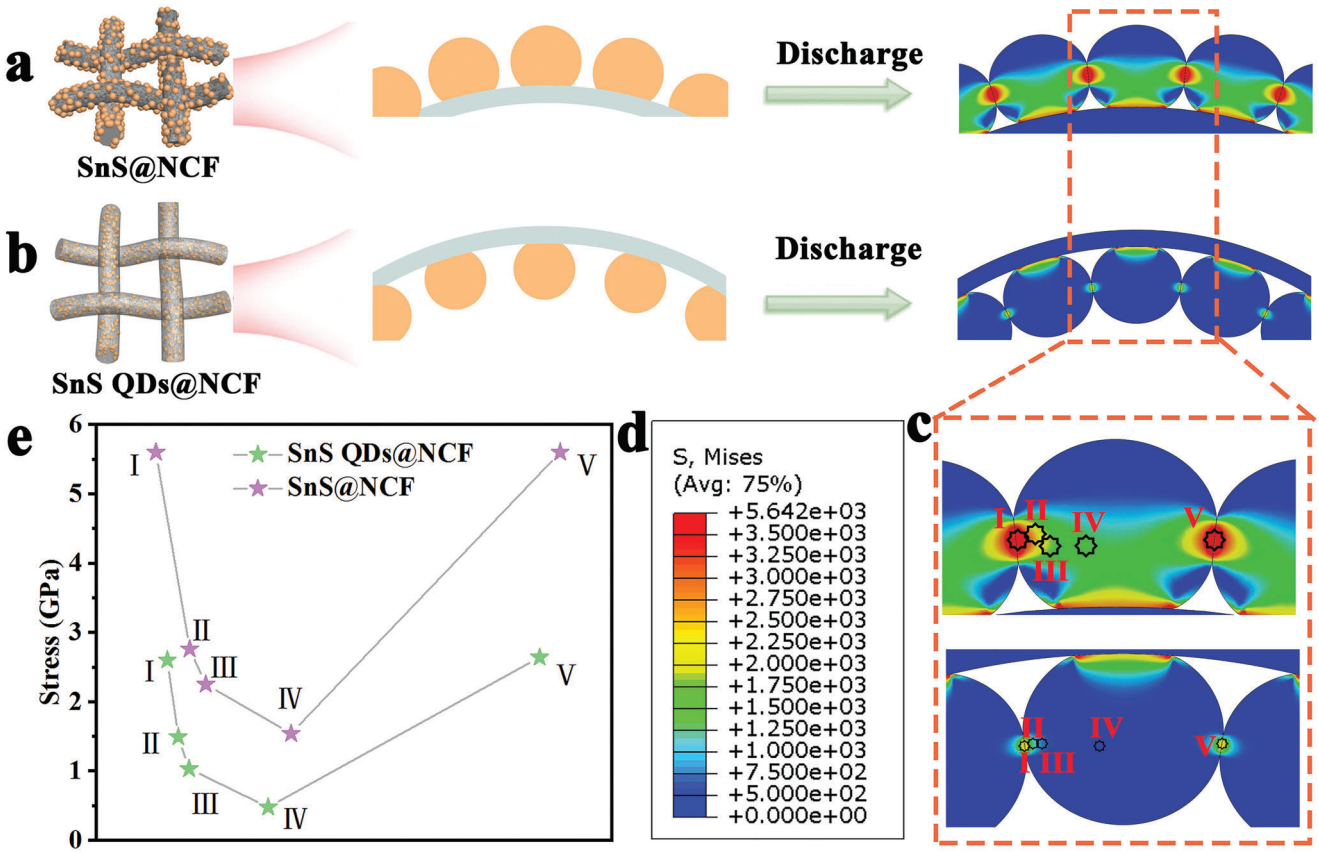

Figure 7. Finite element simulation models of the von Mises stress distribution during sodiation for a) SnS@NCF, b) SnS QDs@NCF, and c) the enlarged rectangular region of (a) SnS@NCF and (b) SnS QDs@NCF. d) The stress colormap e) comparison of maximum stress at various sites for two samples.

process, respectively. It is obvious that SnS@NCF performs the high and inhomogeneous stress concentration on the contacted surface of adjacent particles after sodiation process, resulting in damaged structure. In contrast, SnS QDs@NCF displays much smaller and more homogeneous stress on the contact surface than that of SnS@NCF. Besides, Figure 7e shows that the stress at various contact sites in SnS QDs@NCF is less than SnS@NCF, which indicate that the well-dispersed QDs confined in carbon fibers can relieve volumetric expansion. Besides, the stress of the contact surface in SnS@NCF is higher than its internal stress, whereas in SnS QDs@NCF, the variation in stress at different sites is much reduced. Therefore, SnS QDs@NCF performs a more uniform stress distribution and less contact stress compared with SnS@NCF, demonstrating an excellent structural stability during long-term cycling process.

Following the excellent performances in half cells, we continued to test the performance of the SnS QDs@NCF anode in a full SIB with $Na_3V_2(PO_4)_3$/C as the cathode. The voltage window for this full cell is set between 0.5 and 3.8 V. The cycle life of the full battery is shown in **Figure 8**a, where after 150 cycles at 1.0 A g^{-1}, the discharge capacity of 200 mAh g^{-1} was achieved with Coulombic efficiency of 99.58%. The rate performance of the full cell (Figure 8b,c) gradually degrades from 0.1 to 5 A g^{-1}, as expected. After a discharge current density of 5 A g^{-1}, the capacity comes back to 187.5 mAh g^{-1} at a current density of 1 A g^{-1}, demonstrating the stability of the anode material. And the energy output of this battery is sufficient to power a light-emitting diode (LED) (Figure 8d). Based on these results, the SnS QDs@NCF electrode can be a potential candidate as the anode material for sodium-ion batteries.

3. Conclusion

In summary, a novel SnS QDs@NCF was delicately designed and rationally fabricated in pursuit of higher structural stability and capacity for NIBs via a facial LiN_3-assisted electrospinning method. The nucleus of Sn-sources is prevented from agglomerating and growing into large particles with the addition of LiN_3 during the decomposition process, resulting in quantum scale SnS nanocrystalline confined within N-doped carbon fibers. The unique structure can effectively accommodate the volume change and retain structural integrity during ultrafast sodiation/desodiation process, demonstrating superior long-term cycling stability. It displays a reversible capacity of 484.6 mAh g^{-1} after 5800 cycles 2 A g^{-1}. At a relatively high current density as high as 10 A g^{-1}, the SnS QDs@NCF electrode still delivers a high capacity of 430.9 mAh g^{-1} after 7880 cycles with a coulombic efficiency of almost 100%, demonstrating superior long-term life span and excellent rate performance. It is also revealed the enhanced capacitive-controlled process and promoted Na^+

© 2023 Wiley-VCH GmbH

16136829, 0, Downloaded from https://onlinelibrary.wiley.com/doi/10.1002/smll.202302188 by Fudan University, Wiley Online Library on [03/06/2023]. See the Terms and Conditions (https://onlinelibrary.wiley.com/terms-and-conditions) on Wiley Online Library for rules of use; OA articles are governed by the applicable Creative Commons License

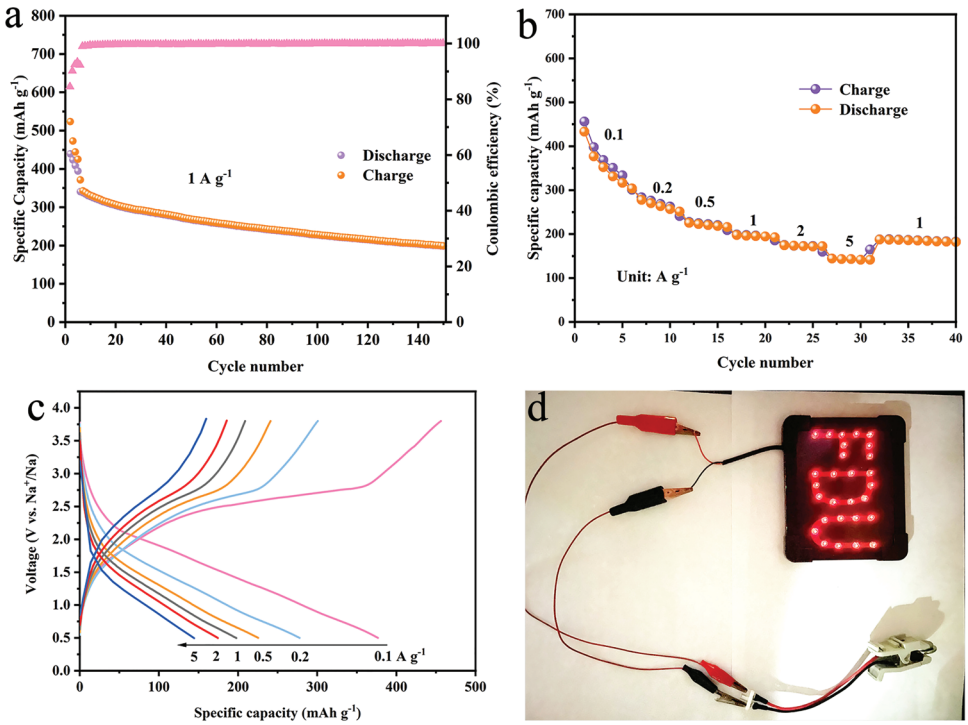

Figure 8. a) Cycling performances, b) rate performances, and c) discharge/charge profiles at various current densities (based on the anode mass) of NVP//SnS QDs@NCM full cells. d) Digital image of red LEDs lit by one NVP//SnS QDs@NCF full cells.

diffusion coefficients by the analysis of the electrochemical kinetics benefiting from the well-dispersed SnS QDs in the nanofibers. This work provides an alternative strategy for the design and fabrication of quantum dots active materials encapsulated in the N-doped carbon fibers for high energy storage.

4. Experimental Section

Synthesis of SnS QDs@NCF Composites: In a typical synthesis, polyacrylonitrile (PAN, 0.4 g) and polyvinyl–pyrrolidone (PVP, 0.4 g) were first dissolved into *N, N*-dimethylformalde (DMF, 10 ml) under vigorous stirring at 80 °C oil bath for 12 h until a homogeneous solution was formed. A certain amount of $SnCl_2 \cdot H_2O$ and metal amide powders (LiN_3, 10% in term of PVP/PAN weight) were then added to the above solution and continuously stirred for 6 h at room temperature. The above solution was loaded into a 10 mL plastic syringe with a stainless steel needle. The flow rate was kept at 0.3 mL h^{-1}, the distance between needle and collector was 15 cm, and the applied voltage was 16 kV. The as-spun nanofibers precursors were dried at 60 °C for 8 h in vacuum to remove the residual DMF solvent. Subsequently, the nanofibers were heated and stabilized to 250 °C for 2 h with a temperature ramp of 2 °C min^{-1} in a muffle furnace. Then the fibers with amount of sulfur powders were transferred to tuber furnace, which were placed into two ceramic boats separately, the ceramic boats contained sulfur powders were placed in the upstream. They were heated up to 500 °C for 2 h with a heating rate of 2 °C min^{-1} under H_2/N_2 gas. After cooling down to the room temperature, the black product was obtained (SnS QDs@NCF).

Synthesis of SnS@NCF Composites: SnS@NCF composites were prepared in a similar process with SnS QDs@NCF except that the LiN_3 powders were absent.

Material Characterization: The morphology and microstructure of the as-synthesized fibers were characterized using an FE-SEM (JEOL, Tokyo, Japan) and Energy-filtered TEM (JEOL 7500FA, Tokyo, Japan). The crystal structure was determined by X-ray powder diffraction (XRD, D8 Advance, Bruker AXS) with Cu Kα (λ = 1.5406 nm) at a scan rate of 10°C min^{-1}. Raman data was collected on a Horiba Evolution with 532 laser source. The composition of fibers was determined using thermogravimetry analysis (TGA, Netzsch STAM 449 F3). X-ray photoelectron spectra (XPS, Perklin Elmer PHI 5000 C ESCA) was carried out to investigate the surface elemental states of fibers.

Electrochemical Characterization: The electrode was prepared by mixing active material (70 wt.%), Super P carbon black (20 wt.%), as well as carboxymethyl cellulose (CMC, 10 wt.%) in deionized water, the obtained homogeneous slurry was pasted onto copper foil, then drying at 80 °C for 12 h under vacuum. The half-cell of NIBs with 2032 type coin cell were assembled in a glove box under Ar (water and oxygen concentration were <0.1 ppm), the as-prepared electrode and sodium foil were used as anode and counter electrode, respectively. $NaClO_4$ (1.0 M) in propylene carbonate (PC) solution with 5% fluoroethylene carbonate (FEC) was used as electrolyte. Galvanostatic tests were performed on a LAND battery tester in a voltage of 0.01–3.0 V at room temperature, specifically, the current density and specific capacity were tested based on the total mass of the composites. Besides, for the long-term cycling performances under high current density (2 or 10 A g^{-1}), all electrodes were first activated for three cycles at a current density of 100 mA g^{-1} and then tested at high current density for NIBs. To assemble full cells, $Na_3V_2(PO_4)_3$/C cathode material was used. The electrode was prepared by grinding, $Na_3V_2(PO_4)_3$/C Super P and PVDF in a weight ratio of 7:2:1 in *N*-methyl-2-pyrrolidone (NMP) and coated onto an aluminum foil. Then, the materials were oven dried at 80°C for 12 h. The full cell was assembled based on the capacity ratio of ≈1.2:1 between cathode and the SnS QDs@NCF anode. The voltage window for this full cell was set between 0.5 and 3.8 V An activation pretreatment was carried out for SnS QDs@NCF by applying three-times of discharge–charge cycles in half cells before assembling into full cells. The cyclic voltammetry (CV) and the electrochemical impedance spectroscopy (EIS) were conducted on the electrochemical workstation (CHI 660E), in which EIS was tested in the frequency of 100 kHz to 0.01 Hz.

 © 2023 Wiley-VCH GmbH

16136829, 0, Downloaded from https://onlinelibrary.wiley.com/doi/10.1002/smll.202302188 by Fudan University, Wiley Online Library on [03/06/2023]. See the Terms and Conditions (https://onlinelibrary.wiley.com/terms-and-conditions) on Wiley Online Library for rules of use; OA articles are governed by the applicable Creative Commons License

Finite Element Modeling: To simulate the stress distribution of SnS@NCF and SnS QDs@NCF, finite element models were established using Abaqus 6.14. Two models were built to simulate the tightly packed particles on fiber surface in SnS@NCF and the well-dispersed SnS QDs confined within fibers in SnS QDs@NCF, respectively. The Yong modulus and Poisson ration of the nanoparticles were set as 46.9, −0.91, 21.1, and −0.23 GPa in the direction of *X* and *Y*, respectively. In order to observe the stress change of the contact surface, the outside boundary displacement was restricted in all directions, and the thermal expansion was used instead of the sodiation-induced expansion.

Supporting Information

Supporting Information is available from the Wiley Online Library or from the author.

Acknowledgements

This work was partially supported by the National Natural Science Foundation of China (51971065 and 51901045) and the Innovation Program of Shanghai Municipal Education Commission (2019-01-07-00-07-E00028).

Conflict of Interest

The authors declare no conflict of interest.

Data Availability Statement

The data that support the findings of this study are available in the supplementary material of this article.

Keywords

long-term cycling lifetimes, Na-ion batteries, tin sulfide quantum dots, ultrahigh rates

Received: March 15, 2023
Revised: May 1, 2023
Published online:

[1] J. W. Choi, D. Aurbach, *Nat. Rev. Mater.* **2016**, *1*, 16013.
[2] N. Ortiz-Vitoriano, N. E. Drewett, E. Gonzalo, T. Rojo, *Energy Environ. Sci.* **2017**, *10*, 1051.
[3] M. T. McDowell, S. W. Lee, W. D. Nix, Y. Cui, *Adv. Mater.* **2013**, *25*, 4966.
[4] J. Y. Hwang, S. T. Myung, Y. K. Sun, *Chem. Soc. Rev.* **2017**, *46*, 3529.
[5] J. Zheng, Y. Yang, X. Fan, G. Ji, X. Ji, H. Wang, S. Hou, M. R. Zachariah, C. Wang, *Energy Environ. Sci.* **2019**, *12*, 615.
[6] D. Liu, L. Yang, Z. Chen, G. Zou, H. Hou, J. Hu, X. Ji, *Sci. Bull.* **2020**, *65*, 1003.
[7] B. Jia, Q. Yu, Y. Zhao, M. Qin, W. Wang, Z. Liu, C.-Y. Lao, Y. Liu, H. Wu, Z. Zhang, X. Qu, *Adv. Funct. Mater.* **2018**, *28*, 1803409.
[8] W. Wang, B. Jiang, C. Qian, F. Lv, J. Feng, J. Zhou, K. Wang, C. Yang, Y. Yang, S. Guo, *Adv. Mater.* **2018**, *30*, 1801812.
[9] M. G. Boebinger, D. Yeh, M. Xu, B. C. Miles, B. Wang, M. Papakyriakou, J. A. Lewis, N. P. Kondekar, F. J. Q. Cortes, S. Hwang, X. Sang, D. Su, R. R. Unocic, S. Xia, T. Zhu, M. T. McDowell, *Joule* **2018**, *2*, 1783.
[10] Y. Zhao, J. Zhu, S. J. H. Ong, Q. Yao, X. Shi, K. Hou, Z. J. Xu, L. Guan, *Adv. Energy Mater.* **2018**, *8*, 1802565.
[11] G. Ma, X. Xu, Z. Feng, C. Hu, Y. Zhu, X. Yang, J. Yang, Y. Qian, *Nano Res.* **2020**, *13*, 802.
[12] X. Xiong, C. Yang, G. Wang, Y. Lin, X. Ou, J.-H. Wang, B. Zhao, M. Liu, Z. Lin, K. Huang, *Energy Environ. Sci.* **2017**, *10*, 1757.
[13] R. Lv, J. A. Robinson, R. E. Schaak, D. Sun, Y. Sun, T. E. Mallouk, M. Terrones, *Acc. Chem. Res.* **2014**, *48*, 56.
[14] Z. Wei, L. Wang, M. Zhuo, W. Ni, H. Wang, J. Ma, *J. Mater. Chem. A* **2018**, *6*, 12185.
[15] L. Wang, X. Li, Z. Jin, Z. Liang, X. Peng, X. Ren, B. Gao, G. Feng, P. K. Chu, K. Huo, *J. Mater. Chem. A* **2019**, *7*, 27475.
[16] S. Shi, C. Sun, X. Yin, L. Shen, Q. Shi, K. Zhao, Y. Zhao, J. Zhang, *Adv. Funct. Mater.* **2020**, *30*, 1909283.
[17] R. Mo, Z. Lei, K. Sun, D. Rooney, *Adv. Mater.* **2014**, *26*, 2084.
[18] R. Mo, D. Rooney, K. Sun, H. Y. Yang, *Nat. Commun.* **2017**, *8*, 13949.
[19] D. Chao, C. Zhu, P. Yang, X. Xia, J. Liu, J. Wang, X. Fan, S. V. Savilov, J. Lin, H. J. Fan, *Nat. Commun.* **2016**, *7*, 12122.
[20] J. Shi, Y. Wang, Q. Su, F. Cheng, X. Kong, J. Lin, T. Zhu, S. Liang, A. Pan, *Chem. Eng. J.* **2018**, *353*, 606.
[21] T. Zhou, W. K. Pang, C. Zhang, J. Yang, Z. Chen, H. K. Liu, Z. Guo, *ACS Nano* **2014**, *8*, 8323.
[22] S. H. Choi, Y. C. Kang, *Nano Res.* **2015**, *8*, 1595.
[23] L. Wu, H. Lu, L. Xiao, J. Qian, X. Ai, H. Yang, Y. Cao, *J. Mater. Chem. A* **2014**, *2*, 16424.
[24] C. Zhu, P. Kopold, W. Li, P. A. van Aken, J. Maier, Y. Yu, *Adv. Sci.* **2015**, *2*, 1500200.
[25] C. Chen, L. Wang, Y. Liu, Z. Chen, D. Pan, Z. Li, Z. Jiao, P. Hu, C.-H. Shek, C. L. Wu, *Langmuir* **2013**, *29*, 4111.
[26] H. Gao, T. Zhou, Y. Zheng, Q. Zhang, Y. Liu, J. Chen, H. Liu, Z. Guo, *Adv. Funct. Mater.* **2017**, *27*, 1702634.
[27] Z. Huang, B. Liu, D. Kong, Y. Wang, H. Yang, *Energy Storage Mater.* **2018**, *10*, 92.
[28] M. Y. Ye, Z. H. Zhao, Z. F. Hu, L. Q. Liu, H. M. Ji, Z. R. Shen, T. Y. Ma, *Angew. Chem., Int. Ed.* **2017**, *56*, 8407.
[29] J. Yang, L. Xi, J. Tang, F. Chen, L. Wu, X. Zhou, *Electrochim. Acta* **2016**, *217*, 274.
[30] S. J. Yang, S. Nam, T. Kim, J. H. Im, H. Jung, J. H. Kang, S. Wi, B. Park, C. R. Park, *J. Am. Chem. Soc.* **2013**, *135*, 7394.
[31] R. Wang, M. Han, Q. Zhao, Z. Ren, C. Xu, N. Hu, H. Ning, S. Song, J.-M. Lee, *Electrochim. Acta* **2017**, *243*, 152.
[32] C. Peng, B. Chen, Y. Qin, S. Yang, C. Li, Y. Zuo, S. Liu, J. Yang, *ACS Nano* **2012**, *6*, 1074.
[33] E. G. S. Firmiano, M. A. L. Cordeiro, A. C. Rabelo, C. J. Dalmaschio, A. N. Pinheiro, E. C. Pereira, E. R. Leite, *Chem. Commun.* **2012**, *48*, 7687.
[34] G. Xia, L. Zhang, F. Fang, D. Sun, Z. Guo, H. Liu, X. Yu, *Adv. Funct. Mater.* **2016**, *26*, 6188.
[35] Z. Yuan, L. Dong, Q. Gao, Z. Huang, L. Wang, G. Wang, X. Yu, *J. Alloys Compd.* **2019**, *777*, 775.
[36] Y. Liu, N. Zhang, L. Jiao, J. Chen, *Adv. Mater.* **2015**, *27*, 6702.
[37] K. N. Kudin, B. Ozbas, H. C. Schniepp, R. K. Prud'homme, I. A. Aksay, R. Car, *Nano Lett.* **2008**, *8*, 36.
[38] P. Pachfule, D. Shinde, M. Majumder, Q. Xu, *Nat. Chem.* **2016**, *8*, 718.
[39] Q. Guo, Y. Ma, T. Chen, Q. Xia, M. Yang, H. Xia, Y. Yu, *ACS Nano* **2017**, *11*, 12658.
[40] M. Wang, H. Xu, Z. Yang, H. Yang, A. Peng, J. Zhang, J. Chen, Y. Huang, X. Li, G. Cao, *ACS Appl. Mater. Interfaces* **2019**, *11*, 41363.
[41] D. Li, L. Dai, X. Ren, F. Ji, Q. Sun, Y. Zhang, L. Ci, *Energy Environ. Sci.* **2021**, *14*, 424.
[42] X. Hu, J. Chen, G. Zeng, J. Jia, P. Cai, G. Chai, Z. Wen, *J. Mater. Chem. A* **2017**, *5*, 23460.

 © 2023 Wiley-VCH GmbH

16136829, 0, Downloaded from https://onlinelibrary.wiley.com/doi/10.1002/smll.202302188 by Fudan University, Wiley Online Library on [03/06/2023]. See the Terms and Conditions (https://onlinelibrary.wiley.com/terms-and-conditions) on Wiley Online Library for rules of use; OA articles are governed by the applicable Creative Commons License

[43] J. Cao, C. Chen, Q. Zhao, N. Zhang, Q. Lu, X. Wang, Z. Niu, J. Chen, *Adv. Mater.* **2016**, *28*, 9629.
[44] Y. Hou, J. Li, X. Gao, Z. Wen, C. Yuan, J. Chen, *Nanoscale* **2016**, *8*, 8228.
[45] P. Wang, D. Zhao, X. Hui, Z. Qian, P. Zhang, Y. Ren, Y. Lin, Z. Zhang, L. Yin, *Adv. Energy Mater.* **2021**, *11*, 2003069.
[46] J. Ruan, T. Yuan, Y. Pang, S. Luo, C. Peng, J. Yang, S. Zheng, *Carbon* **2018**, *126*, 9.
[47] G. Huang, F. Zhang, X. Du, Y. Qin, D. Yin, L. Wang, *ACS Nano* **2015**, *9*, 1592.
[48] B. Sun, Q. Zhang, C. Zhang, W. Xu, J. Wang, G. Yuan, W. Lv, X. Li, N. Yang, *Adv. Energy Mater.* **2021**, *11*, 2100082.
[49] Z. Sang, X. Yan, D. Su, H. Ji, S. Wang, S. Dou, J. Liang, *Small* **2020**, *16*, 2001265.
[50] P. He, Y. Fan, X. Yu, X. Lou, *Angew. Chem.* **2017**, *129*, 12370.
[51] Q. Pan, M. Zhang, L. Zhang, Y. Li, Y. Li, C. Tan, F. Zheng, Y. Huang, H. Wang, Q. Li, *ACS Nano* **2020**, *14*, 17683.
[52] H. Li, Y. He, Y. Dai, Y. Ren, T. Tao, G. Zhou, *Chem. Eng. J.* **2022**, *427*, 131784.
[53] Z. Zhou, Q. Wang, J. Yan, K. Zhu, K. Ye, G. Wang, D. Cao, *ACS Nano* **2021**, *15*, 12140.
[54] X. Shi, Y. Gan, Q. Zhang, C. Wang, Y. Zhao, L. Guan, W. Huang, *Adv. Mater.* **2021**, *33*, 2100837.
[55] G. Zhang, X. Ou, J. Yang, Y. Tang, *Small Methods* **2021**, *5*, 2100374.
[56] H. Zhang, Y. Cheng, Q. Zhang, W. Ye, X. Yu, M. Wang, *ACS Nano* **2021**, *15*, 10107.
[57] D. Chao, P. Liang, Z. Chen, L. Bai, H. Shen, X. Liu, X. Xia, Y. Zhao, S. V. Savilov, J. Lin, Z. Shen, *ACS Nano* **2016**, *10*, 10211.
[58] Y. Zhang, P. Chen, Q. Wang, Q. Wang, K. Zhu, K. Ye, G. Wang, D. Cao, J. Yan, Q. Zhang, *Adv. Energy Mater.* **2021**, *11*, 2101712.
[59] G. K. Veerasubramani, M. S. Park, J. Chio, D. Kim, *ACS Appl. Mater. Interfaces* **2020**, *12*, 7114.
[60] L. Li, Y. Ma, F. Cui, Y. Li, D. Yu, X. Lian, Y. Hu, H. Li, S. Peng, *Adv. Mater.* **2023**, *35*, 2209628.

© 2023 Wiley-VCH GmbH

16136829, 0, Downloaded from https://onlinelibrary.wiley.com/doi/10.1002/smll.202302188 by Fudan University, Wiley Online Library on [03/06/2023]. See the Terms and Conditions (https://onlinelibrary.wiley.com/terms-and-conditions) on Wiley Online Library for rules of use; OA articles are governed by the applicable Creative Commons License